Interference Drag Modeling and Experiments for a High Reynolds Number Transonic Wing

Kyle C.D. Knight,[1,a] Eric M. Braun,[2,b] Christopher J. Roy,[3,a] Frank K. Lu,[4,b] Joseph A. Schetz[5,a]

[a]*Virginia Tech, Blacksburg, VA, 24061*
[b]*University of Texas at Arlington, Arlington, Texas, 76019*

Multidisciplinary Design Optimization (MDO) studies show the Strut/Truss Braced Wing (SBW/TBW) concept has the potential to save a significant amount of fuel over conventional designs. For the SBW/TBW concept to achieve these reductions, the interference drag at the wing strut juncture must be small compared to other drag sources. Computational Fluid Dynamics (CFD) studies have indicated that the interference drag is small enough to be manageable. However, the RANS formulation and turbulence models used in these studies have not been validated for high Reynolds number transonic junction flows. This study assesses turbulence models by comparing flow separation characteristics obtained from experiment and CFD. The test model used is a NACA 0012 wing of aspect ratio 2 at Mach number of 0.76 and a Reynolds number of 6 million with varying angle of attack. The CFD study involved an 18.8 million cell structured grid of the wind tunnel test section using the ANSYS Fluent 12.0 solver. The k-ω SST turbulence model was the main turbulence model employed. Experiments were conducted in a high Reynolds number transonic Ludwieg tunnel. The wing was tested at different Mach numbers and inlet conditions to account for some of the experimental variations. Porous walls eliminate shock reflection across the tunnel. Surface oil flow visualization is used to indicate the interference flow patterns. The assessment shows CFD overpredicts separation and therefore interference drag, likely due to deficiencies in the turbulence model.

Nomenclature

AoA = Angle of attack
BC = Boundary Condition
C_D = Drag coefficient

---

[1] Graduate Research Associate, Department of Aerospace and Ocean Engineering, Student Member AIAA

[2] Graduate Research Associate, Aerodynamics Research Center, Department of Mechanical and Aerospace Engineering, Box 19018. Student Member AIAA.

[3] Associate Professor, Department of Aerospace and Ocean Engineering, Associate Fellow AIAA.

[4] Professor and Director, Aerodynamics Research Center, Department of Mechanical and Aerospace Engineering, Box 19018. Associate Fellow AIAA.

[5] Fred D. Durham Chair, Department of Aerospace and Ocean Engineering, Life Fellow AIAA.

American Institute of Aeronautics and Astronautics

C_L = Lift coefficient
EFD = Experimental Fluid Dynamics
ε_{IE} = Iterative Error
f = System Response Quantity
F_s = Factor of Safety
h = Grid spacing parameter
M = Mach number
MDO = Multidisciplinary Design Optimization
N = Number of grid cells
p = Order of Accuracy
p_S = Static pressure
p_T = Total pressure
RANS = Reynolds-Averaged Navier–Stokes
r = Refinement factor
Re = Reynolds number
SBW = Strut Braced Wing
SSV = Sliding sleeve valve
TBW = Truss Braced Wing
t = Time
U_{DE} = Uncertainty due to Discretization Error
U_{IE} = Uncertainty due to Iterative Error
U_N = Uncertainty due to Numerical Error
x = Streamwise coordinate
y = Spanwise coordinate
z = Wall normal coordinate
γ = Specific heat ratio

I. Introduction

Current airliners incur significant financial and environmental costs from fossil fuel consumption, pollution generation at high altitude, and noise production during takeoff. Designers are currently considering revolutionary configuration changes to alleviate these problems. Several leading configuration changes include hybrid flying wings, non-body of revolution fuselages, and strut or truss braced wings (SBW/TBW). MDO studies show the SBW/TBW can reduce fuel consumption by up to 20%.[1]

The SBW/TBW configuration has several technical challenges to overcome before it can be considered a viable design option. One of the concerns is interference drag generated at wing-strut and strut-strut junctions in the transonic regime. Interference drag is the extra drag produced when two aerodynamic bodies are in close proximity.[2] There is little experimental data available for thin struts under transonic conditions. Previous RANS CFD studies have estimated interference drag[3,4] for strut-strut and strut-wall junctures. However, turbulence models used in these studies have not been thoroughly validated for high Reynolds number, transonic junction flows. This study assesses turbulence models by comparing computational results with high Reynolds number, transonic wind tunnel experiments for an idealized junction flow.

CFD and Experimental Fluid Dynamics (EFD) have a history of working together for junction flows. Notably, compression pylons were designed using Euler codes.[5,6,7] These CFD designs were then analyzed via experiment and then modified to achieve design goals. Another

study by Jones and Clarke compared EFD and CFD data for a wing body junction at low Mach and Reynolds numbers.[8] This study used the same solver and turbulence models used in this study.

II.   Experimental Facilities, Model, and Test Conditions

The wind tunnel used in this study is a high Reynolds number, transonic Ludwieg tunnel that was originally developed as a prototype design option for the NASA National Transonic Facility.[9] High Reynolds numbers are obtained by filling the charge tube of the tunnel with air up to 5 MPa, whereby the stagnation pressure after the starting expansion wave can reach 3.5 MPa during a test. This prototype remained a competitive option for the National Transonic Facility until the cryogenic tunnel concept was proven to be feasible. The main benefit from this design is minimal disturbances to the test section flow. Drawbacks include relatively short run times and high forces generated on test models.

Figure 1 shows a schematic of the tunnel. Prior to a run, the entire tube is filled with high pressure air which will correspond with a desired test section Reynolds number. An unsteady expansion wave is initiated by rapidly opening a sliding-sleeve valve (SSV) located at the end of the tunnel. As the wave travels though the charge tube, steady flow can theoretically be generated in the test section for 185 milliseconds. The charge tube is round, and a nozzle with a contraction ratio of 2.27 transitions to a rectangular test section measuring 18.5 cm (height), 23.2 cm (width), and 60 cm (length). Although the contraction ratio is fixed, the test section Mach number can be varied by keeping a certain portion of 27 ports open on the SSV to adjust the mass flow rate exhausted. The test section also utilizes porous walls to eliminate reflected shock waves. The tunnel Mach number ranges from 0.5–1.2. The Reynolds number can be independently varied between 2.03-20.32 million for a model of 5.08 cm chord (40-400 million per meter).
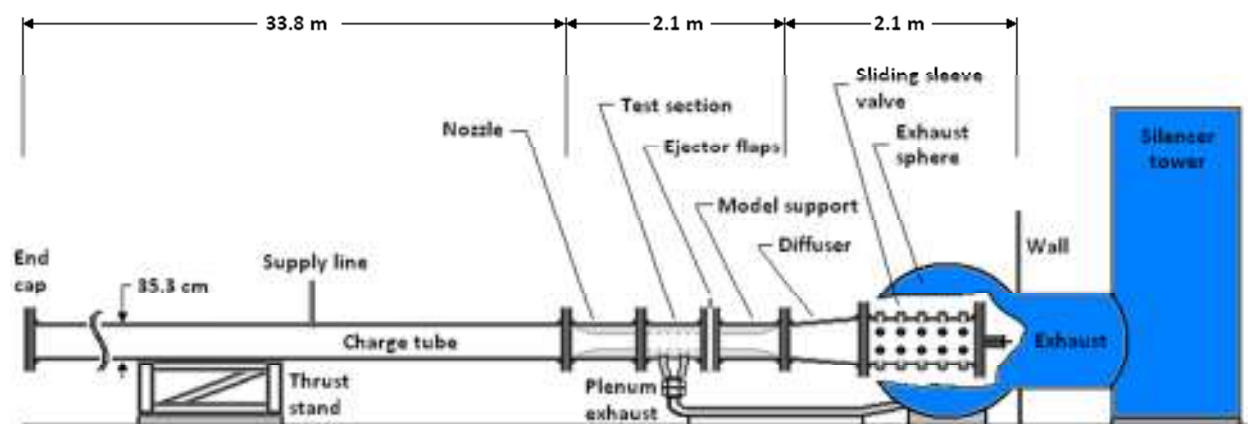

Figure 1.   Schematic of the transonic Ludwieg tunnel indicating length scales and major components.

The tunnel is equipped with instrumentation in the charge tube, plenum area, and test section. A thermocouple and Pitot probe are mounted along the wall of the charge tube to measure flow conditions prior to the nozzle. Four static pressure ports are located in each side of the plenum chamber. A pressure measurement on each side can be used to indicate if the air is flowing

3
American Institute of Aeronautics and Astronautics

uniformly though the porous walls, and all four can be utilized to estimate the test section Mach number. As proven by centerline probe tests, the Mach number difference between the test section and plenum chamber flow is usually negligible. However, a difference can occur if the ejector flaps and porous walls are adjusted to settings that result in low mass removal.[11] Figures 2 and 3 show results from a typical run with a Reynolds number of about 6 million. The starting expansion wave lasts about 50 ms before flow conditions become steady. The reflected expansion wave then ends the run at $t = 0.28$ seconds. The Reynolds and Mach numbers remain steady during the run time.
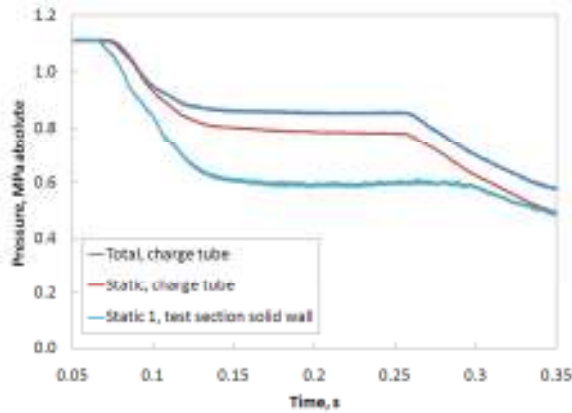

Figure 2.   Typical pressure traces in the charge tube and test section.
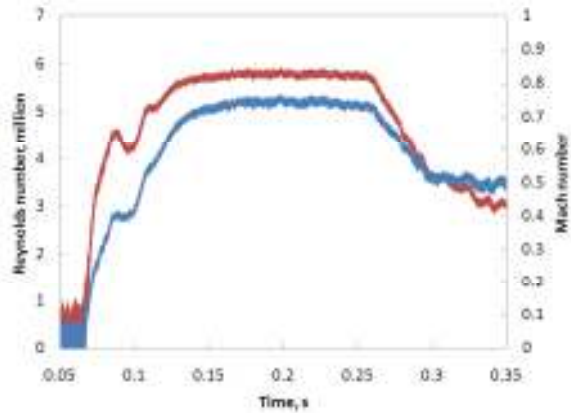

Figure 3.   Typical Reynolds and Mach number traces.

The top and bottom walls are porous while the side walls are solid. The solid walls ensure interference effects near the fin are not disturbed. Furthermore, the solid walls contain 3 inch diameter ports for access to the test section from outside the tunnel. These ports provide a dual purpose of optical access or housing a 5-component force balance. Wing models can be mounted on the balance such that they are flush with the surface of the solid wall. Shock waves produced by the model are then absorbed by the porous walls on the top and bottom. An optical port blank is placed across from the force balance to maintain symmetry. Since the addition of two solid plates has the potential to create a difference in the test section and plenum chamber Mach numbers, static pressure ports were added at several locations along the wall opposite of the wing.
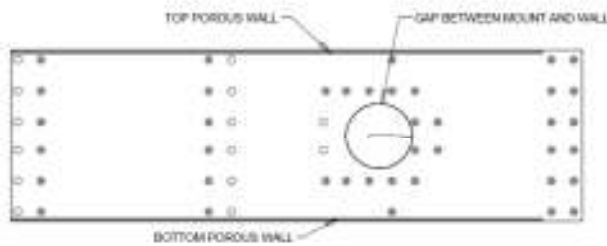

Figure 4. Geometry of the test condition.

Figure 5.   Photograph of the installed model.

The model in the test section is a NACA 0012 unswept wing with an aspect ratio of 2.0 and a chord of 5.08 cm (2"). The wing span is 10.16 cm (4"), or 43.7% of the width of the test section. The wing is attached perpendicular to the test section wall and AoA is varied from 0° to

4

American Institute of Aeronautics and Astronautics

7°. The region of interest is where the wing meets the wall. Interference effects are expected in this "interaction region."

Figures 4 and 5 show the NACA 0012 model test setup. It has been fitted to a disk with a diameter of slightly less than three inches which connects to the balance. The force balance is free to rotate in the optical port before being tightened down, allowing for the AoA to be adjusted easily. The AoA is measured using a digital level and a reference surface attached to the balance. Due to the high force exerted on the model during the run, a small gap between the disk and the wall is required to allow the balance to flex without interfering with measurements. However, most of the experimental data in this study was collected with the wing on the wall opposite to what is shown in Fig. 5 since it does not have a gap.

To determine regions of separated flow,[14] surface oil flow visualization is utilized to indicate flow patterns on the model caused by interference with the wall. Note the interference effects occur on the leeward side of the wing. The short-duration, high shear conditions create a need for a high viscosity oil mixture that will move with the airflow during the test time, but not so much during subsequent expansion wave reflections. Oil flow dots, in particular, have been used since they form narrow streaks that indicate the flow streamlines. The dot size ensures that the oil will flow for a limited distance. Arrays of dots of different color patterns are painted in a spanwise direction along the wing. The mixture used consists of roughly 70% oil paint and 30% SAE 85W-140 gear oil.

A second surface flow visualization option uses a fluorescent oil mixture since it can result in high-contrast images.[15] The mixture is created by grinding fluorescent chalk and adding it to a light transmission fluid. Trial-and-error testing showed that the chalk must be ground through a 100 micrometer filter so as not to interfere with the surface flow results. The mixture appears slightly grainy on the surface, whereby the flow direction can be established. It also must be applied as a thin film. Images of these techniques appear in Figure 6. Note the tip streamlines turn inward due to lift, but interference from the wall is minimal.

Figure 6. Images of surface oil flow visualization techniques with regular and fluorescent mixtures.

A. Test Condition

The validation study intends to match the conditions of a strut meeting a wing at 40 kft (12.2 km) and M=0.85.[1] Preliminary CFD tests show the tunnel choking at this Mach number. Reducing the Mach number to $M = 0.76$ prevents choking. This is above the critical Mach number for a NACA 0012, so the flow maintains transonic effects. The Reynolds number for a

1.0 meter strut at this altitude is ~6 million. The parameters for this test are $M = 0.76$ and Re = 6×10^6.

III. Computational Methods

The CFD study is performed using the 3D compressible Reynolds-Averaged Navier–Stokes (RANS) equations. Two equation turbulence models are employed: the Wilcox 1998 k-ω model and Menter k-ω SST.[12,13] The equations are discretized via a finite volume method for compressible flow[12] using a Roe second order upwind discretization scheme. The flow solver is the commercial CFD software ANSYS/Fluent[TM] 12.0. The grid family of four systematically refined grids is produced to determine the effect of grid resolution. The parameter h, defined in Equation (1), is used to describe the differences in grid resolution. Table 1 shows the number of cells in the grids along with their h values.

$$h = \left(\frac{N_{Coarse}}{N_{Fine}}\right)^{1/3} \tag{1}$$

Table 1. Grid cells and corresponding h parameters used for this study.

Grid Cells	h
700 K	4.00
5.75 M	2.00
18.8 M	1.33
44.4 M	1.00

The boundary conditions applied are solid walls, inlet conditions, and outlet conditions. Solid walls employ no slip parallel to the wall and no flow perpendicular to the wall. The inlet conditions specify a stagnation pressure and stagnation temperature and flow direction. Outlet conditions specify static pressure and direction of flow normal to the boundary.

Fully modeling the UTA tunnel is beyond the capability of our computational and time resources. The domain of interest is reduced to the test section, and the walls are assumed to be solid, which reduces complexity and simplifies the physics. Velocity in the x-direction for the test section inlet conditions are available[9] for when the test starts and finishes. The CFD simulation models the tunnel start and finish conditions by introducing boundary layers of different thicknesses at the tunnel entrance. The boundary layer profile is extrapolated from previous data at similar conditions.[9,16] The walls are always modeled as solid, but were angled out in some tests to test flow sensitivity to porous wall effects.

System Response Quantities

The system response quantities (SRQs) used in this study are limited to those that can be measured experimentally. The data obtained in the experiment are oil flow visualizations on the leeward side of the wing. A good assessment of the turbulence models is how well they predict the separation region. A qualitative comparison method is visually comparing experimental oil flow visualizations to near-surface streamlines created from simulations, seen in Figure 7. A more rigorous method is comparing specific measurements of the separation zone. These measurements are the start of separation from the leading edge (LE), the maximum span of the separation zone (Max Span), and the span of the separation zone at a specific chord length. The chord length is chosen where there is a grid line so there is no interpolation error. For parametric

American Institute of Aeronautics and Astronautics

studies this location is chosen to be 88.8% chord. A graphic representation of these SRQs can be seen in Figure 8.
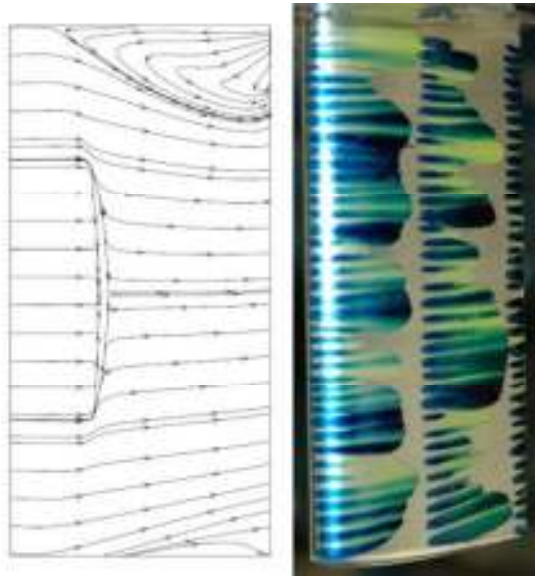

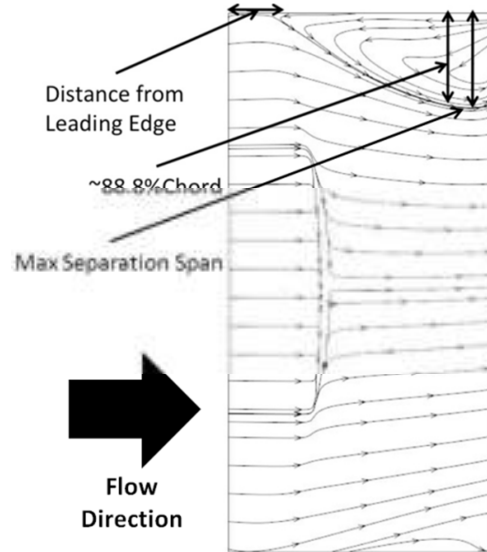**Figure 7. Streamlines from CFD versus experimental oil flow visualization.**

Figure 8. Measurements of separation metrics.

Uncertainty Quantification

Code verification ensures the algorithms are implemented properly. Verification studies have been performed on Fluent[TM] for the 2-D Euler equations and k-ω SST model.[17] The Euler equations were verified using the exact solution to Ringleb's flow and approached second order accuracy. The k-ω SST model was tested for a flat plate using a code to code comparison. The comparison used NASA's verified CFL3D and FUND3D codes.[18] The Fluent[TM] solutions are in close agreement with, and asymptote toward, the flat plate solutions.

Solution verification assesses the numerical errors of the simulation. The numerical errors for this study are iterative and discretization error. Iterative error is defined as the difference between the current approximate solution to the discretized equations and the exact solution to the discretized equations.[19] For this study iterative error is estimated by keeping a history of the drag as the solution converges. The iterative error at each point is calculated using Equation (2) where $C_{D,\text{Iteration}}$ is the drag at iteration i and C_{D_Final} is the drag at the final iteration. Note this does not give good estimates near the final iteration. Iterative error is assessed well before the final iteration and is estimated to be below 0.1% for all cases.

$$\varepsilon_{IE} = \left| \frac{C_{D\_Iteration} - C_{D\_Final}}{C_{D\_Final}} \right| \tag{2}$$

Discretization error (DE) is defined as the difference between the exact numerical solution and the exact solution of the governing equations. The Grid Convergence Index GCI[18] is used to estimate the uncertainty due to the discretization error. Equation (3) shows the version of the GCI used in this study. F_s is the factor of safety, r is the refinement factor, p is the order of accuracy, and f_i is a system response quantity on grid level i.

$$U_{DE} = \frac{F_s}{r^p - 1}|f_2 - f_1| \tag{3}$$

The total estimated numerical uncertainty (U_N) is seen in Equation (4). The U_N is estimated at the extents of possible AoA, 0° and 5°, and can be seen for all the SRQs can be seen in Tables 2 and 3. A $F_s = 3.0$ was employed along with $p = 2.0$

$$U_N = U_{IE} + U_{DE} \tag{4}$$

Table 2. Total estimated numerical uncertainty for AoA 0°.

SRQ	Fine Grid Value	Numerical Uncertainty (%)
C_D	0.00413	2.89
LE (x/c)	0.8284	1.26
SpanMax (z/b)	6.536E-3	0.23
Span@0.986 (z/b)	6.536E-3	0.23

Table 3. Total estimated numerical uncertainty for AoA 5°.

SRQ	Fine Grid Value	Numerical Uncertainty (%)
C_D	0.01578	6.62
LE (x/c)	0.1491	37.84
SpanMax (z/b)	0.1599	3.14
Span@0.986 (z/b)	0.1567	2.50

There are two main types of uncertainty, aleatory and epistemic. Aleatory uncertainty is an uncertainty which is due to inherent randomness. The typical probability distribution is a normal or Gaussian distribution, though there are others. Epistemic uncertainty is when the uncertainty is due to a lack of knowledge. Here we treat epistemic uncertainty using intervals with no associated probability distribution.[19]

For real world applications there is a mixture of aleatory and epistemic uncertainties. This study has narrowed down the identified model input uncertainties to changes in freestream Mach number and tunnel wall boundary layer growth as the test runs. Of these quantities, Mach number is treated as an aleatory uncertainty while boundary layer growth is treated as an epistemic uncertainty. The experiments report that the uncertainty in the Mach number is normally distributed with a mean of M = 0.75+/-0.02 with two standard deviations. The boundary layer grows over time and is treated as an epistemic uncertainty. The interval limits are smallest and largest boundary layers heights, which occur at the beginning and ending of the run respectively.

A Cumulative Distribution Function (CDF) is one method of characterizing the uncertainty in a SRQ. The CDF is the integral of the Probability Density Function (PDF).[19] A comparison between the two can be seen in Figure 10. The CDF is read as a cumulative probability that a value is less than or equal to a given value. For example, in Figure 10 the cumulative probability that the thermal conductivity is less than or equal to 0.6 W/m °C is 50%. In many cases there may be a nonlinearity in the SRQs as they are being sampled for the CDF. The place where the behavior changes is called a bifurcation point. This study has such a case. For certain AoA the separation behavior in the interaction region can change rapidly with small changes in Mach number. An example of such behavior is seen in Figure 11. An example CDF produced by such behavior is seen in Figure 12.

A probability box, or p-box, results when aleatory and epistemic uncertainties are propagated through a model. For this study, epistemic uncertainty is reduced to only two boundary layer conditions and aleatory uncertainty is reduced to Mach number. Multiple runs with all other

conditions held the same, except for the Mach number, show a linear relationship between Mach number and the SRQs.
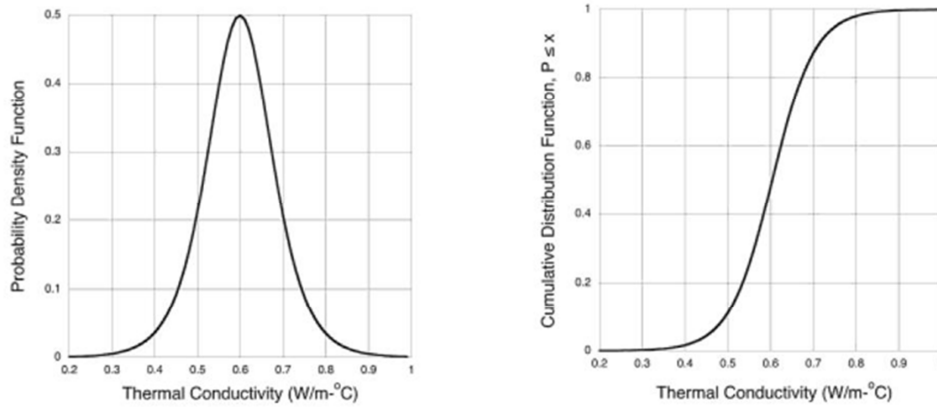

Figure 10. Example of a PDF and CDF from Oberkampf and Roy[19]

This is not true at the bifurcation point where SRQs change rapidly. For this case the bifurcation point is well defined and an interpolation between the closest points is employed. This creates a surrogate model for the SRQs as a function of Mach number. The p-box bounds are produced by propagating the aleatory Mach number uncertainty through the model at both the beginning and ending tunnel boundary conditions.
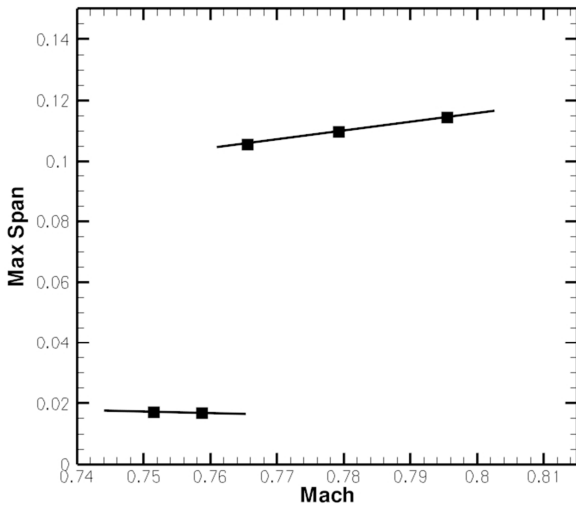
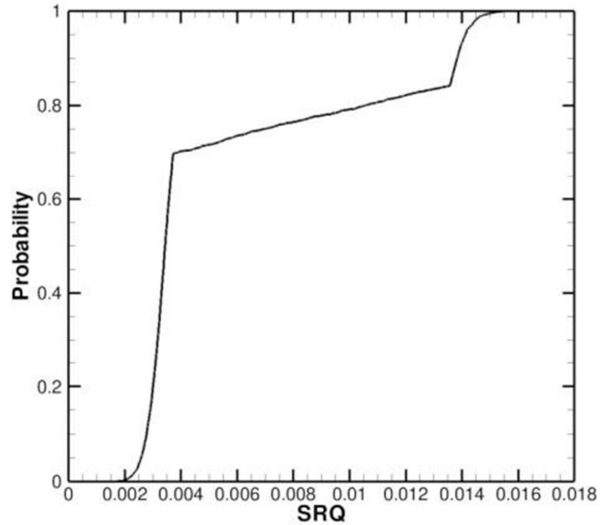**Figure 11. The Maximum Separation SRQ demonstrating linear behavior before and after M=0.76.**

Figure 12. Example of a CDF with a bifurcation point.

Turbulence Model Comparison

A study was executed to determine how different turbulence models performed using a 5.8 million cell grid at AoA 3° and 4°. The study shows the k-ω and Spalart-Allmaras models comparing well with the k-ω SST.[12]

American Institute of Aeronautics and Astronautics

Interference Drag Calculations

   It is important to isolate the drag in the interaction region. It is assumed that the drag will increase when a large separation zone appears. If this is shown in the CFD prediction it will support this assumption. A major limitation of this SRQ is that it cannot be compared to experimental measurements. The estimation of interference drag is performed by breaking the wing into different segments as seen in Figure 13. The segments are the left, center, and right where the drag is dominated by induced drag (left), nominal 2-D drag (center), and interference drag (right) respectively. The center of the span is assumed to be 2-D, though we might see different behavior if the wing extended across the test section. The right segment is exposed to the side wall boundary layer. This means there is a lower Mach number and therefore lower drag. The interference drag is calculated using Equation (5) where $D_{interference}$ is the actual interference drag, D_i is the drag on the segment i, and S_i is the surface area of the segment i.

   The interference drag is studied at AoA 3$^{\text{o}}$ by adjusting the Mach number. A slight change in Mach number produces a large difference in the size of the separated zone. The coefficient of interference drag is estimated by the total calculated interference drag and using the reference area of chord squared (c^2), as employed by Duggirala, et al.[4] For low separation $C_{D_{int}} = -0.0017$. This value is negative due to the large boundary layer which decreases the apparent Mach number near the wall. For large separation $C_{D_{int}} = 0.0022$. The difference between these is $\Delta C_{D_{int}} = 0.0039$ or 39 drag counts.

$$D_{int} \approx D_R - \frac{S_R}{S_C} D_C \qquad (5)$$

IV. Results

   Figure 14 shows how the separation zone and strong shock are predicted to vary with AoA. The Mach number and entrance boundary layer were the same: M=0.75 and the smaller tunnel start boundary layer. For AoA 3$^{\text{o}}$, the separation zone in the interaction region is very small. There is some slight separation behind the strong shock, but it has a maximum height of 0.03 mm. As the AoA increases to 4$^{\text{o}}$, the strong shock and separation zone in the interaction region get much larger and change behavior. The separation zone moves toward the leading edge and widens near the trailing edge. The strong shock becomes more symmetrical due to the larger separation zone. The separation behind the strong shock becomes larger and symmetrical, but does not change height. Below AoA 3$^{\text{o}}$ the separation zone and shock strength continue to decrease. Above AoA 4$^{\text{o}}$ the shock strength grows while the separation zone in the interaction region does not change significantly.

   Figure 15 shows streamlines near the surface obtained from CFD along with experimental data for the separation zone. At AoA 3$^{\text{o}}$ the shock is apparent from the recirculation zone along with disturbances in the streamlines. The recirculation zone in the interaction region is apparent, but small. The experimental data compare well qualitatively with the simulation. As the AoA raises to 4$^{\text{o}}$ the shock is pushed outward on the span. The CFD results predict the recirculation zone becoming much larger and moving upstream toward the leading edge. The experimental data do not show much change in the separation zone. There is no longer a good qualitative comparison. Quantitatively, the shock location and leading edge separation point are close to the CFD simulation.
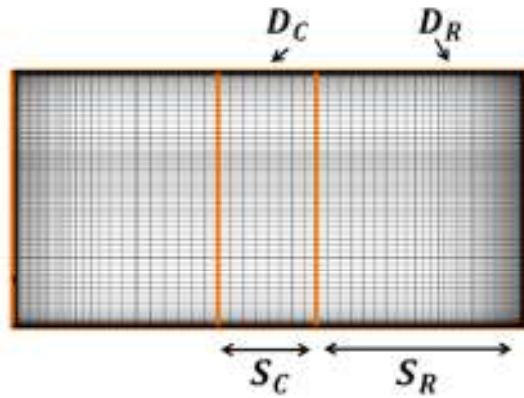
Figure 13. The breakdown of the wing computationally into left, center, and right components.
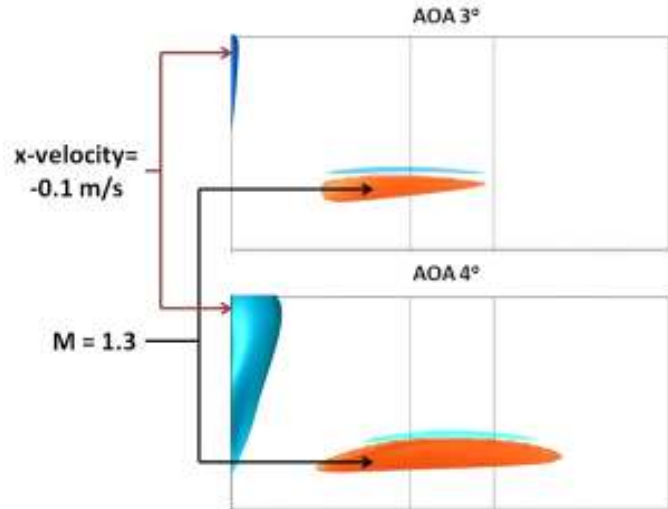
Figure 14. CFD predictions at AoA 3° and 4° showing isosurfaces of strong shocks (M=1.3) and separation (x-velocity = -0.1 m/s). Re= 6 million, freestream Mach is 0.75.
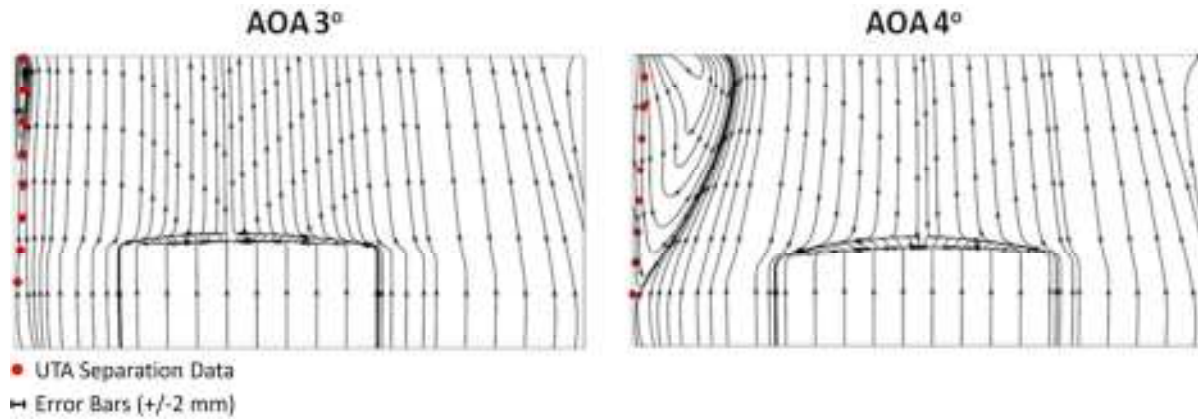

- UTA Separation Data
- Error Bars (+/-2 mm)

Figure 15. AoA 3° and 4° with streamlines from CFD simulations and separation zone data points obtained from experiments.

The parametric study involves numerous simulations to assess the flow at various AoA, Mach numbers, and inlet conditions. This provides a better comparison with experimental data by accounting for some of the known wind tunnel uncertainties, specifically changes in Mach number and boundary layer growth.

The experimental data is taken at M = 0.76+/-0.02 and has a normal distribution. This distribution can be replicated in the simulation by sampling from the Mach number CDF to create a CDF of the SRQs. The entrance boundary layer variation is accounted for by running the simulation at the starting and ending conditions, resulting in two CDFs. The numerical uncertainty from the grid study is included by subtracting the numerical uncertainty from the lower of the two CDFs and adding the numerical uncertainty to the higher valued CDF. This creates a p-box for each of the SRQs.

The C_D has not been measured experimentally so only the numerical uncertainty could be assessed. The C_D has a relatively moderate numerical uncertainty compared to epistemic uncertainty as seen in Figure 16. Figure 17 shows the LE SRQ agrees poorly with experimental

American Institute of Aeronautics and Astronautics

data, though the experimental data is within the relatively large numerical uncertainty. The maximum separation SRQs, Figures 18 and 19 show good agreement before the separation becomes very large. AoA 3° shows a small model form uncertainty, while AoA 4° has large model form uncertainty.
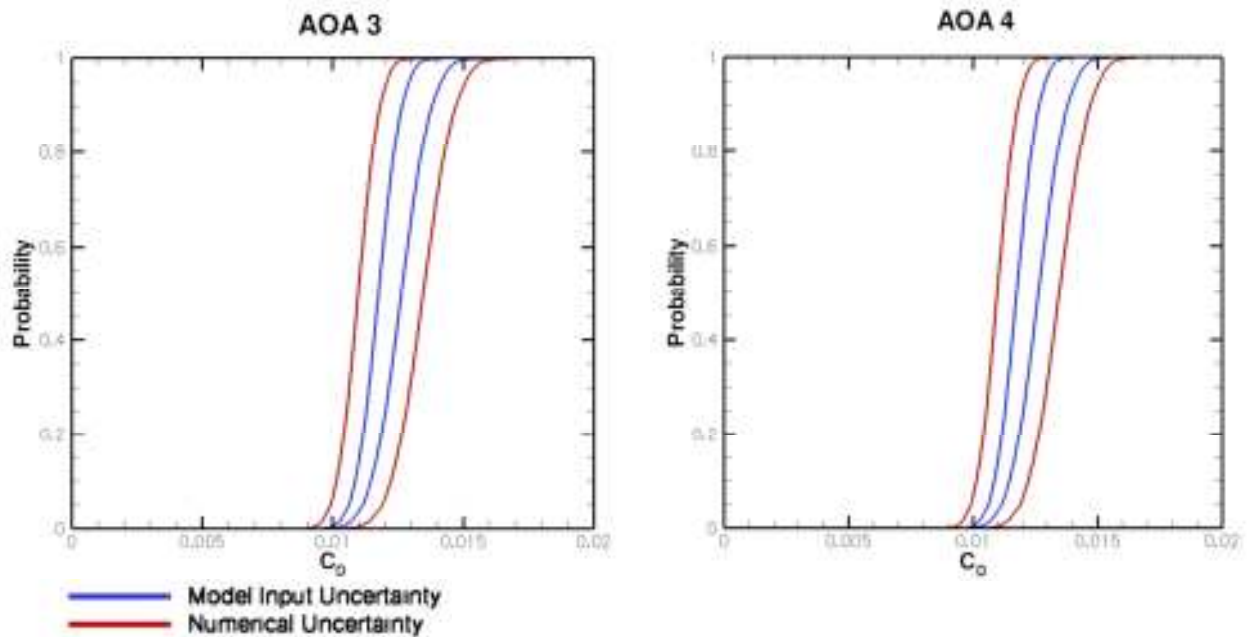

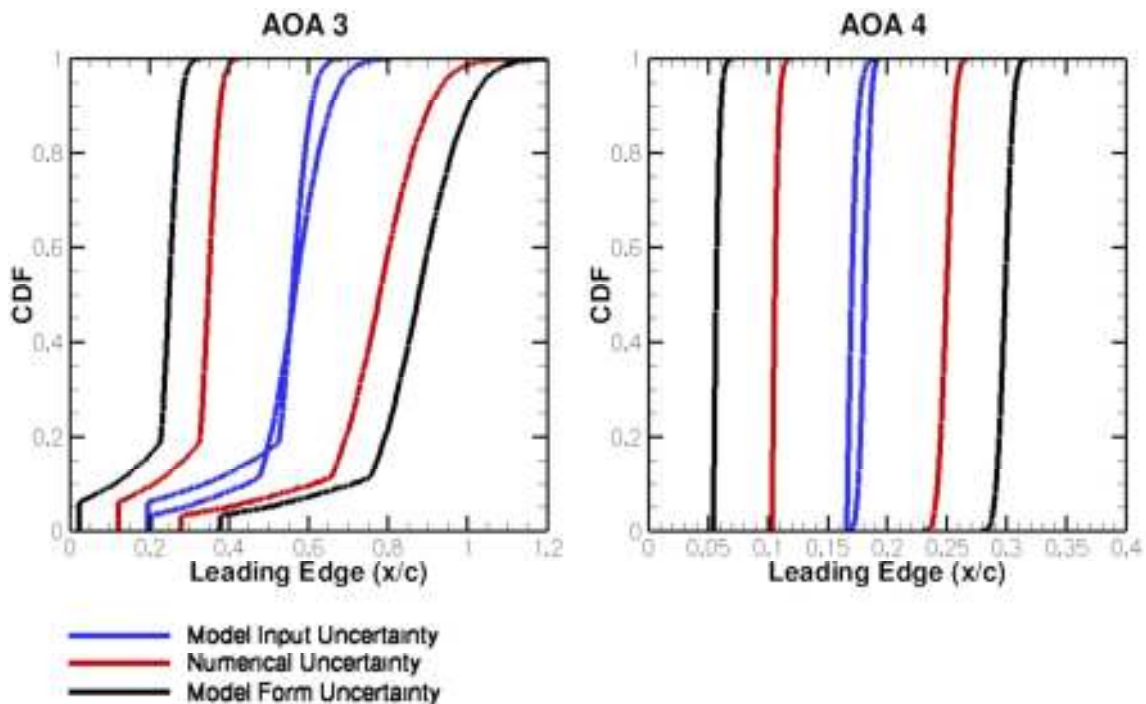**Figure 16. Coefficient of drag p-boxs for AoA 3° and 4°, respectively.**

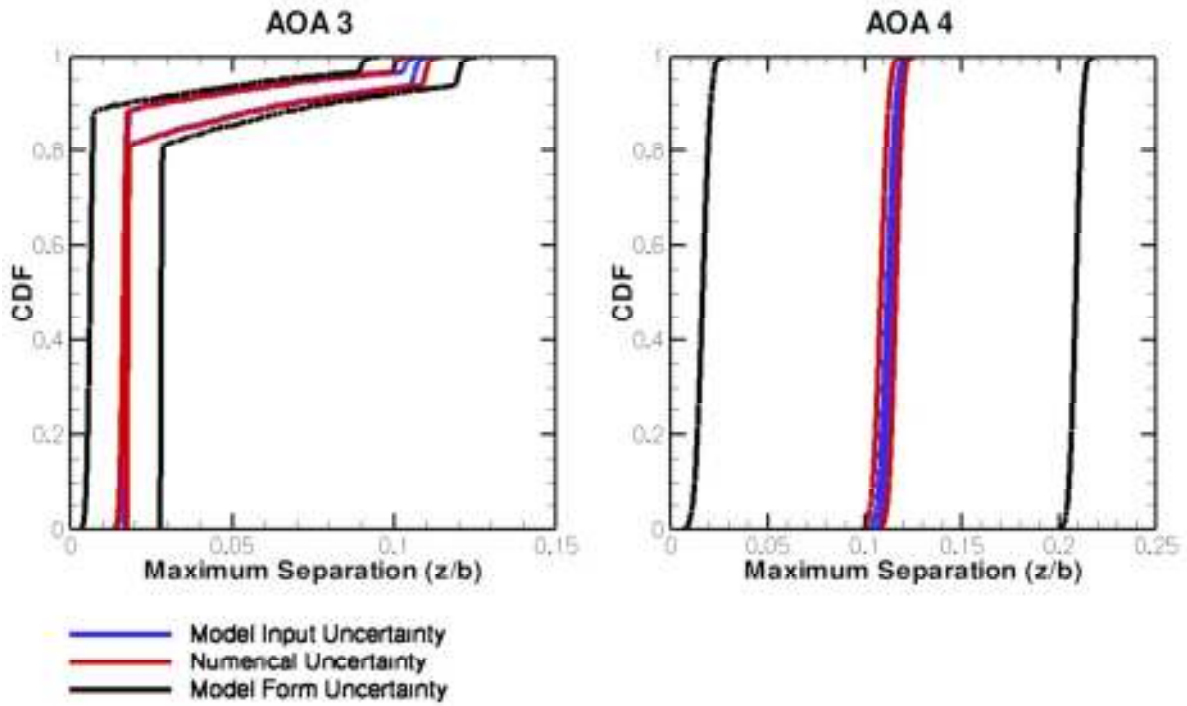**Figure 17. Leading edge SRQ p-boxs for AoA 3° and 4°, respectively.**

American Institute of Aeronautics and Astronautics

Figure 18. Maximum separation SRQ p-boxs for AoA 3° and 4°, respectively.
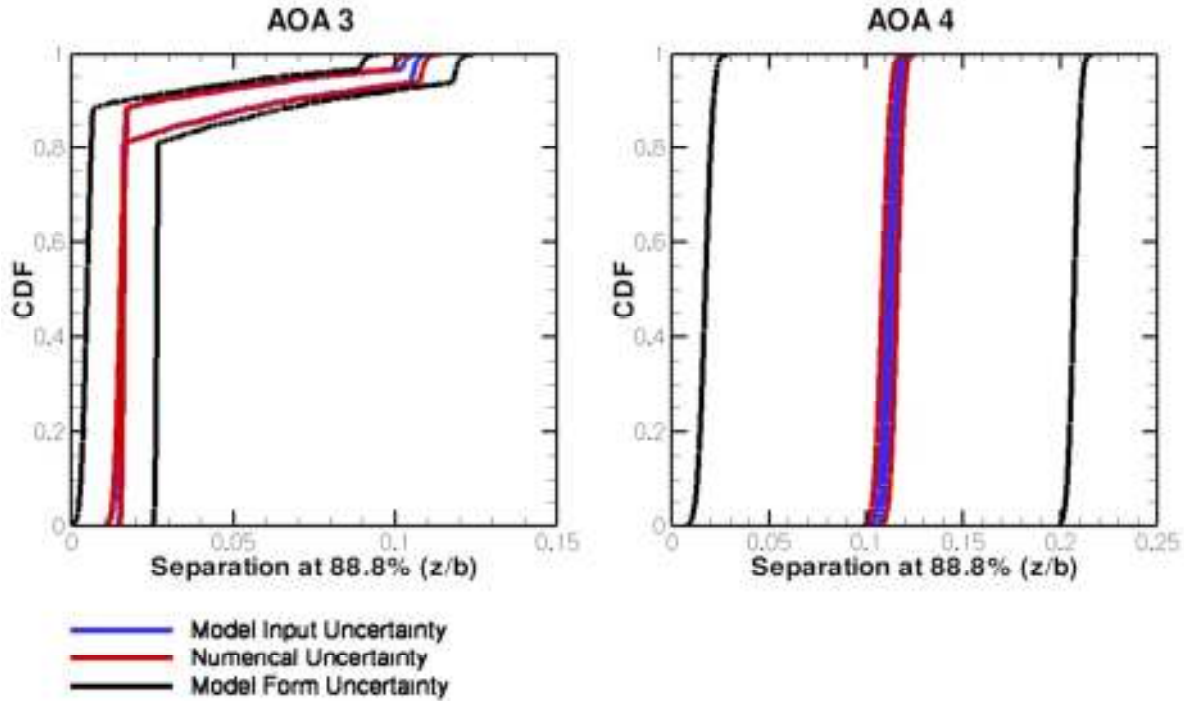
Figure 19. Separation at 88.8% SRQ p-boxs for AoA 3° and 4°, respectively.

American Institute of Aeronautics and Astronautics

Porous Wall Modeling

An assumption of solid walls was made early in the CFD study. A more intensive study of how porous walls affect SRQs is required. The experimentalists measured Mach number at three locations at or near the centerline of the tunnel across from the NACA 0012 fin. These experimental measurements were compared against the computational centerline Mach number results. And example of this data is seen in Figure 20. Note the discrepancy between CFD and experiment at x/c = 0. Though mostly linear, the CFD shows a small bump in this region while the experiment does not confirm this. The local porous wall behavior was not able to be replicated in CFD and may alleviate separation. More investigation of the local porous wall behavior is necessary.

AoA 7° Case

The experimental AoA was increased to see if a similar separation bubble would appear. Larger separation was observed at an AoA 7°. As seen in Figure 21 the separation zone is now visible and large for the experiment. Figure 21 also shows the CFD prediction, which has larger separation behind the shock and in the junction with the wall. Propagation of the aleatory and epistemic uncertainties was not performed due to time constraints, but a comparison between the two was possible. Table 5 shows the changes in the SRQs. Qualitatively, the AoA 7° experiment is much closer to the CFD prediction. Quantitatively, the shock location and leading edge starting point are close, but the other SRQs remain far apart.

Table 5. Comparison of SRQs between CFD and Experiment for Wall Angling for AoA 7°.

SRQs	LE (x/c)	Max Span (y/b)
Experiment	0.3750	0.0648
CFD Prediction	0.0989	0.1462
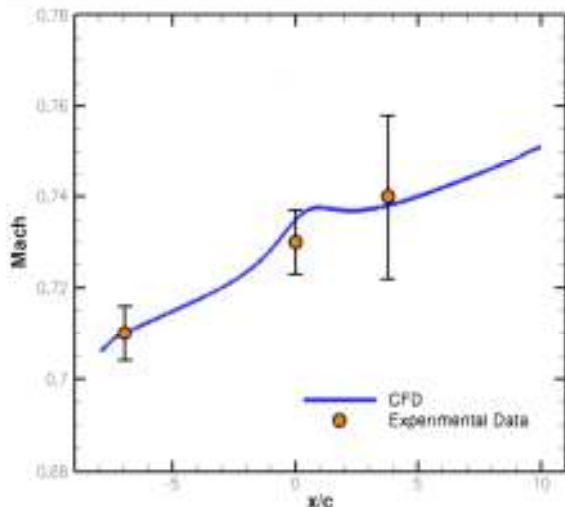
Figure 20. Mach centerline measurements of experiment and CFD for AoA 7°.
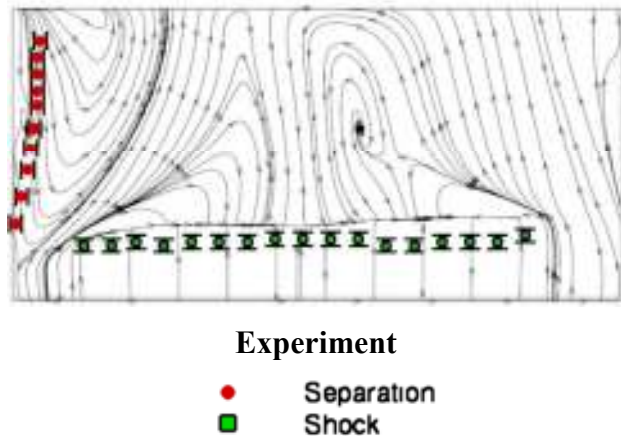

Experiment

● Separation
□ Shock

Figure 21. Comparison of CFD prediction and oil flow visualization at AoA 7°.

V. Conclusions

This study assessed turbulence models for high Reynolds number, transonic junction flows. How well the turbulence models predict separation in these flows was the main question addressed. The geometry for the simulations is a wind tunnel with a rectangular cross-section. A NACA 0012 wing was placed in the test section and the AoA was varied. The nominal test conditions were a Reynolds number of 6 million and a Mach number of 0.76. CFD predicted a small region of separated flow between the side wall and wing at low AoA (below 3°). Above 3° AoA this separation bubble became very large, stretching across ~10% of the span. The size of the large separation bubble did not vary significantly with increasing AoA.   The experiment showed low separation well past AoA 3°. Only for the 7° AoA was the experimental separation zone significantly larger than in lower AoA.

We also assessed the known aleatory and epistemic uncertainties present in the experimental test. Experimental Mach number variations were treated as an aleatory uncertainty while the boundary layer growth was treated as an epistemic uncertainty. These two uncertainties were propagated through the model to produce p-boxes for the SRQs: separation distance from the leading edge, maximum separation span, and separation span at 88.8% chord. Included in the p-box assessment is the numerical uncertainty, which is mainly composed of discretization uncertainty.   The numerical uncertainty compared to the epistemic uncertainty in tunnel boundary height was moderate for C_D, high for the separation distance from the leading edge, and low for both the maximum separation span and the separation at 88.8% chord.   The experimental and CFD SRQs did not match at high AoA and revealed a large model form uncertainty.

The cause of the large modeling uncertainty is likely due to deficiencies in the turbulence model. While the SRQs show slight sensitivity to porous walls using CFD, RANS turbulence models are known to have trouble predicting separation. It is likely that the differences between experiment and CFD are due to turbulence models. The assessment shows the turbulence model has good agreement before major separation (<AoA 3°) and with the shock location at all times. After major separation (≥AoA 4°) the turbulence model does not agree well with experimental data. At high AoA a separation zone appears in experiment that is qualitatively similar to that seen computationally. The k-ω, k-ω SST, and Spalart-Allmaras turbulence models all produced quite similar results before and after large separation. Since the major separation increases the drag, the turbulence model likely overpredicts the interference drag that will occur in transonic junction flows. Fortunately, this indicates current methods for predicting interference drag based on similar RANS CFD studies[3,4] are conservative and safe to use in MDO studies.

This study concurs with earlier CFD studies by Tetrault et al.[3] and Duggirala, et al.[4] These studies tested wing junctions in the transonic regime between a Reynolds number of 5-6 million. Tetrault et al. studied at M = 0.85 while Duggirala, et al. studied at M=0.85 and M =0.80. The studies produced interference drag counts ranging from 6 to 310. For the closest geometry cases, Tetrault et al. shows 6 interference drag counts and Duggirala et al. shows 54 drag counts, compared to this study's 39 drag counts. Tetrault et al. has low separation in the interaction region while Duggirala et al. has large separation. The interference drag in this study is the difference in drag between the large and small separation case. Measuring interference drag in the same manner as Duggirala et al. and Tetrault et al. produces a negative interference drag for the low separation case due to the oncoming boundary layer. Therefore, the 39 drag counts is due to increased separation. These studies indicate the general trend that low separation

American Institute of Aeronautics and Astronautics

produces drag on the order of 5 drag counts while large separation produces drag on the order of 50 drag counts.

Acknowledgments

References

[1]Gur, O., Bhatia, M., Schetz, J., Mason, W., Kapania, R. and Mavris, D., "Design Optimization of a Truss-Braced Wing Transonic Transport Aircraft," *Journal of Aircraft*, Vol. 47, No. 6, 2010

[2]Hoerner, S., *Fluid Dynamic Drag*, Hoerner, 1965.

[3]Tetrault, P.A., Schetz, J. A., Grossman, B., "Numerical prediction of the Interference Drag of a Streamlined Strut Intersecting a Surface in Transonic Flow," *38th AIAA Aerospace Sciences Meeting and Exhibit*, AIAA Paper 2000-509, 2000.

[4]Duggirala, R., Roy, C. J., Schetz, J. A., "Analysis of Interference Drag for Strut-Strut Interaction in Transonic Flow," *AIAA Journal*, Vol. 49, No. 3, 2011, pp. 449–462.

[5]Chandrasekaran, B., "Computation and Comparison of the Installation Effects of Compression Pylons for a High Wing Transport Aircraft," NASA-16742, January 1988.

[6]Naik, N.A., "Innovative Pylon Concepts for Engine-Airframe Integration for Transonic Transports," *26th AIAA Aerospace Sciences Meeting*, AIAA Paper 88-0004, 1988

[7]Naik, N.A., "Experimental Study of Pylon Cross Sections for Subsonic Transport Airplane," Journal of Aircraft, Vol. 30, No. 5, 1993, pp. 676–681.

[8]Jones, D.A., Clarke, D.B., "Simulation of a Wing-Body Junction Experiment using the Fluent Code," DSTO-TR-1731, June 2005.

[9]Starr, R.F. and Schueler, C.J., "Experimental Studies of a Ludwieg Tube High Reynolds Number Transonic Tunnel," Tech. Rep. AEDC-TR-73-168, Arnold Engineering Development Center, Arnold Air Force Station, TN, Dec. 1973.

[10]Whitfield, J.D., Schueler, C.J., and Starr, R.F., "High Reynolds Number Transonic Wind Tunnels – Blowdown or Ludwieg Type?," *AGARD Fluid Dynamics Panel Specialists' Meeting on Facilities and Techniques for Aerodynamic Testing at Transonic Speeds and High Reynolds Numbers*, Göttingen, Germany, April 26–28, 1971.

[11]Kalkhoran, I.M., "An Experimental Investigation of the Perpendicular Vortex-Airfoil Interaction at Transonic Speeds," Ph.D. Dissertation, University of Texas at Arlington, Arlington, TX, 1987.

[12]ANSYS, "ANSYS FLUENT 12.0 User's Guide," 2009

[13]Wilcox, D.C., *Turbulence Modeling for CFD*, 2nd Ed., DCW Industries, La Canada, CA, 1998

[14]Lu, F.K., "Surface Oil Flow Visualization – Still Useful After All These Years," *European Physical Journal – Special Topics*, Vol. 182, No. 1, 2010, pp. 51–63.

[15]Pierce, A.J., Lu, F.K., Bryant, D.S., and Shih, Y., "New Developments in Surface Oil Flow Visualization," *27th AIAA Aerodynamic Measurement Technology and Ground Testing Conference*, AIAA Paper 2010-4353, 2010.

[16]Knight, K. C. D., Roy, C. J., Schetz, J. A. *Assessment of RANS Turbulence Models for Strut-Wing Junctions*, Virginia Tech, May, 2010.

[17]Phillips, T. and Roy, C.J., "Evaluation of Extrapolation-Based Discretization Error and Uncertainty Estimators," *49th AIAA Aerospace Sciences Meeting*, AIAA Paper 2011 (Submitted for Publication)

[18]Rumsey, C., "Turbulence Modeling Resource," Langley Research Center, Virginia, June 2010. [http://turbmodels.larc.nasa.gov/]

[19]Oberkampf, W.L., Roy, C. J. *Verification and Validation in Scientific Computing*, Cambridge University Press, Cambridge, 2010